RSC Sustainability

ROYAL SOCIETY OF CHEMISTRY

PAPER

View Article Online
View Journal | View Issue

Cite this: *RSC Sustainability*, 2025, **3**, 2311

Strategic innovation in CuBTC/PANI nanocomposites for dye remediation: a holistic approach for enhancing adsorption, isotherms, and kinetic studies †

Bhavika Garg,‡ Palkaran Sethi‡ and Soumen Basu*

The environmental persistence of reactive blue 19 dye poses a significant challenge, driving the urgent need for efficient removal technologies to protect water quality. This study introduces a highly effective solution in the form of a copper benzene-1,3,5-tricarboxylate (CuBTC) composite integrated with polyaniline (PANI), designed for the adsorption of Reactive Blue-19 (RB19) dye. The CuBTC/PANI composite was synthesized at varying weight ratios (5%, 10%, and 15%) and meticulously analyzed using a suite of advanced techniques, including FESEM, EDS, FTIR, XPS, XRD, and BET surface area analysis. These characterization studies confirmed the composite's exceptional structural integrity, thermal stability, and high porosity. The adsorption efficiency of the composite was evaluated under various conditions, such as adsorbent dosage, dye concentration, pH, temperature, and contact time. Impressively, the composite achieved a 99% removal efficiency for 60 ppm RB19 at pH 2 within just 50 minutes. Reusability tests highlighted the material's remarkable durability, exhibiting consistent performance over six cycles. Five equilibrium isotherm models were employed to unravel the adsorption process. The Langmuir model ($R^2 = 0.998$) provided the best fit, suggesting that the adsorption process follows a monolayer pattern driven primarily by chemisorption. Post-adsorption FTIR analysis unveiled additional interactions, such as hydrogen bonding, π–π stacking, electrostatic forces, and pore filling, further elucidating the complex adsorption mechanism. Kinetic studies, based on four models revealed that the pseudo-second-order model ($R^2 = 0.990$) best describes the process, with a rate constant of 0.172 mg g^{-1} min^{-1}, indicating that adsorption is governed by a chemical reaction. Thermodynamic analysis indicated that the process is endothermic (ΔH = 795.15 J mol^{-1}) and spontaneous (ΔG = −1.790 kJ mol^{-1}), and results in a decrease in randomness at the solid–liquid interface (ΔS = 3.082 J mol^{-1} K^{-1}). This study provides a comprehensive chemical engineering analysis of the adsorption process, encompassing isotherm, kinetic, and thermodynamic models. The CuBTC/PANI composite emerges as a highly efficient and sustainable material for the removal of RB19, offering not only exceptional adsorption capacity and rapid kinetics but also impressive reusability. This work paves the way for a promising solution in the fight against dye-contaminated wastewater, outshining traditional methods and heralding a new era of water treatment technology.

Received 27th January 2025
Accepted 11th March 2025

DOI: 10.1039/d5su00056d

rsc.li/rscsus

Sustainability spotlight

The contamination of water bodies with synthetic dyes like Reactive Blue 19 poses a severe threat to aquatic ecosystems and human health. Conventional dye removal methods are often energy-intensive, generate secondary pollutants, or lack efficiency at high concentrations. Our study introduces a CuBTC/PANI composite as a sustainable, high-performance adsorbent for efficient dye removal, achieving 99% removal in just 50 minutes with excellent reusability over six cycles. This approach minimizes chemical waste and energy consumption while promoting water resource sustainability. By offering an eco-friendly and cost-effective solution for wastewater treatment, our work aligns with the UN Sustainable Development Goals: Clean Water and Sanitation (SDG 6), Industry, Innovation, and Infrastructure (SDG 9), and Responsible Consumption and Production (SDG 12).

1. Introduction

The extensive application of pigments across various sectors—textile, paper, plastics, leather, food, pharmaceutical, and cosmetics—often results in substantial ecological repercussions. These problems arise from the release of colored waste

Department of Chemistry and Biochemistry, Thapar Institute of Engineering & Technology, Patiala-147004, India. E-mail: soumen.basu@thapar.edu

† Electronic supplementary information (ESI) available: Characterization of the synthesized materials, FTIR, thermodynamic study plot, reusability study plot, and FTIR spectra after 6 cycles of use. See DOI: https://doi.org/10.1039/d5su00056d

‡ Both the authors have equal contribution.

like dyes and pigments into the water bodies.[1–3] Approximately 10–15% of the estimated 700 000 metric tons of dyes generated yearly end up in wastewater. Water contamination is a difficult issue to address, especially since dyes often persist even after conventional removal techniques have been applied.[4,5] Dyes have a lengthy half-life in water reservoirs, which is bad for aquatic life since they block light and oxygen from reaching the water.[6] Furthermore, most of the dyes utilized are harmful; a small amount of these is known to cause human cancer.[7] As a result, cleaning up wastewater contaminated with dyes is a major concern these days.[8–11] The dyeing of cellulosic fibers makes widespread use of Reactive Blue 19, often known as RB19, an anthraquinone-based vinyl sulphone dye. The resonance-stabilized aromatic anthraquinone structure provides it with exceptional resistance to biological and chemical degradation.[12,13] The necessity of removing RB19 from dyeing effluents and wastewater arises from its chemical stability and low biodegradability, which pose significant environmental concerns. Various chemical and physical techniques have been established for wastewater treatment, such as photo-oxidation, ozonation, membrane separation, electrochemical methods, and adsorption. Among these techniques, adsorption stands out due to its numerous advantages: it is non-toxic, adaptable to various types of adsorbents, capable of high adsorption capacities, cost-effective, and achieves substantial removal efficiencies. Adsorption is the most popular choice for treating wastewater due to its remarkable efficiency, user-friendliness, and straightforward design.[14,15] Additionally, this method's renewable nature of adsorbents further enhances its appeal as a sustainable solution for water treatment challenges.[16]

Recently, there has been a notable increase in research aimed at developing materials capable of efficiently adsorbing pollutants from water.[17] Various adsorbents, including natural zeolites, activated carbon, biochar, alumina, and clay minerals, have been used for dye removal. Nonetheless, their effectiveness is limited by issues such as low adsorption capacities, high expenses, and challenges in regeneration. Consequently, there has been a growing focus on exploring low-cost and efficient adsorbents that can be easily regenerated. Conducting polymers, particularly polyaniline (PANI), have recently garnered significant attention for removing aqueous pollutants due to their straightforward synthesis methods, ability to adjust their structures, and versatile functional groups.[17] Polyaniline has demonstrated its effectiveness as an adsorbent in various applications, including the removal of dyes like methyl orange, Acid Green 25, and Acid Violet 49, as seen in the SD/PANI system,[18] polyaniline salts used for Direct Blue 78, and for the removal of crystal violet polyaniline/hollow manganese ferrite nanocomposites.[19] To enhance the number of active sites for adsorption, PANI should be combined with another material having a large surface area like a Metal Organic Framework (MOF).

MOFs are porous materials formed by linking metal clusters or ions with organic linkers through covalent bonds. They possess well-structured crystalline frameworks, significant porosity, and extensive surface areas.[20] These materials, relatively recent in development, find extensive applications in energy storage,[21] adsorption separation,[22] and catalysis.[23] MOFs have been utilized in adsorption applications for both liquid and gas phases and wastewater treatment.[24–26] For example, Haque *et al.* explored the usage of a chromium molecular organic framework to remove MO.[27] The anionic nature of MOs enhances the adsorption capacity and speeds up dye uptake when paired with cationic MOFs.[27] Similarly, MOF-235 and MOF-100 (Fe) have been employed to remove the cationic dye methylene blue (MB), using a similar charge–charge interaction mechanism.[28,29] These applications highlight the versatility of MOFs in addressing environmental challenges associated with dye removal from aqueous solutions.

This study focuses on synthesizing a nanocomposite comprising PANI and CuBTC (MOF). CuBTC due to its high surface area and porosity facilitates effective adsorption processes. The copper centers and organic ligands in Cu-BTC can interact favorably with RB19 dye molecules, enhancing adsorption efficiency. Although Cu-BTC has known stability challenges in aqueous environments, strategies such as compositing with PANI have been employed to enhance its stability. Among various MOFs, Cu-BTC's unique combination of structural properties and potential for enhanced stability through modification made it a suitable choice for investigating the adsorptive removal of RB19 from aqueous solutions.[30–32] The adsorbent samples underwent comprehensive characterization using XRD, FESEM, EDS, FTIR, XPS, and BET techniques. The research explored the impact of various factors including pH, adsorbent dosage, contact time, temperature, and dye concentration on the adsorption process. Furthermore, the study proposed a plausible mechanism for how RB19 interacts and is removed by the nanocomposite. These findings are instrumental in advancing the development of effective treatment methods to eliminate emerging contaminants from wastewater streams.

2. Experiments

2.1 Materials

The materials required for synthesis involve aniline (99%, LOBA CHEMIE), cupric nitrate trihydrate (95%. LOBA CHEMIE), trimesic acid (99%, GLR INNOVATIONS), hydrochloric acid (36%), and ammonium persulfate (98%, SDFCL). The commercial RB19 powder was sourced from Sisco Research Laboratories, and solutions were made by dissolving it in ultrapure double-distilled water and ethanol. Only high-purity, simple reagents were used in the preparation.

2.2 Synthesis of the metal–organic framework (CuBTC)

Initially, 3 mmol of Cu $(NO_3)_2 \cdot 6H_2O$ (0.716 g) was combined with 2 mmol of trimesic acid (0.421 g). Following this, 12 mL of a 1 : 1 ethanol–water solution was added. The mixture was stirred for 30 minutes at room temperature, and then transferred to a muffle furnace and heated at 110 °C for 24 hours. Next, the product was subjected to sonication for 5–10 minutes in a 1 : 1 mixture of ethanol and water. Turquoise-blue crystals

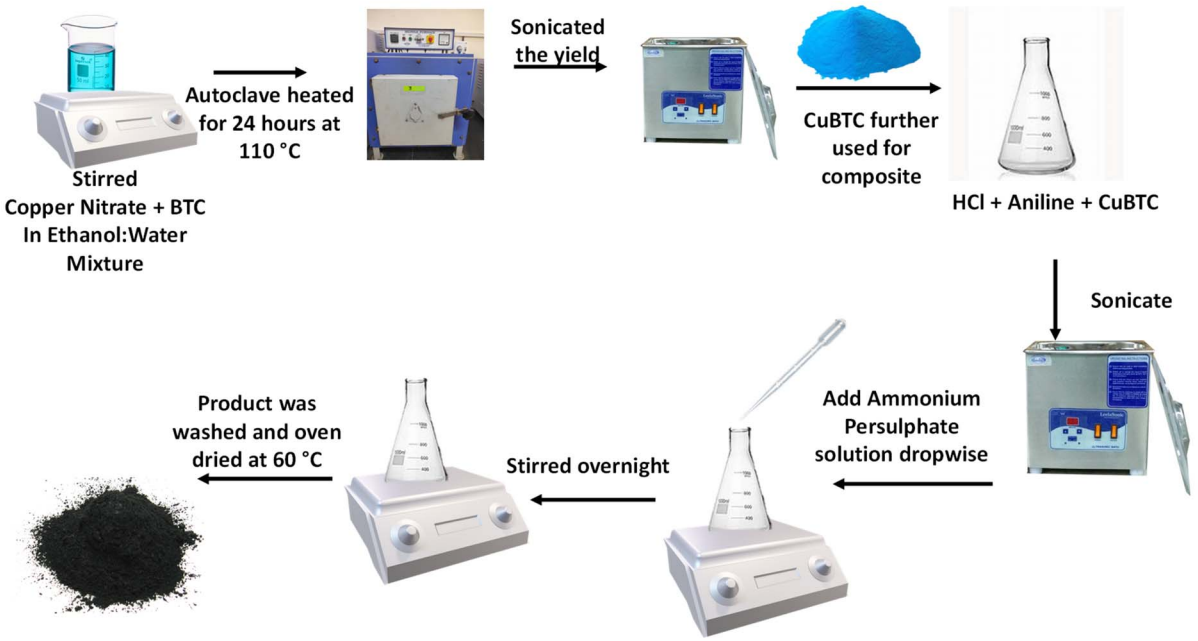

Scheme 1 Synthesis of the PANI/CuBTC photocatalyst.

were then collected using Buchner filtration and allowed to dry in air for one day and were called CuBTC.[33]

2.3 Synthesis of polyaniline (PANI)

50 mL of 2 M HCl and 0.2 mL of aniline were combined in a conical flask. For half an hour, the mixture was mixed. Then, while stirring constantly, 0.5 g of ammonium persulfate ($(NH_4)_2S_2O_8$) in 10 mL of distilled water was added dropwise. For four hours, the reaction was allowed to continue at room temperature. The fluid was then centrifuged for 15 minutes at 5000 rpm. Ethanol and 2 M HCl were used three times to wash the final product. After the finished product was dried for 24 hours at 60 °C in an oven, a green powder known as polyaniline (PANI) was produced.[34]

2.4 Synthesis of the CuBTC/PANI nanocomposite

In three conical flasks, precise amounts of CuBTC were used: 10.5 mg, 22.2 mg, and 35.3 mg, corresponding to 5%, 10%, and 15% weight ratios, respectively. To each flask, 0.2 mL of aniline and 50 mL of 2 M HCl were added to serve as precursors for PANI. The mixtures were sonicated for 30 minutes. Subsequently, a solution of 0.5 g of ammonium persulfate ($(NH_4)_2S_2O_8$) in 10 mL of distilled water was added dropwise while maintaining constant stirring. The reaction was left to run at room temperature for 4 hours. Once completed, the products were centrifuged, rinsed three times with 2 M HCl and distilled water, and then dried in a hot air oven set to 60 °C. The resulting samples were denoted as 5CP, 10CP, and 15CP according to their weight ratios. The synthesis process and images of the CuBTC/PANI hybrid are detailed in Scheme 1.

2.5 Characterization techniques

Details about the characterization methods can be found in Section S1 of the ESI.†

2.6 Adsorption experiments

The nitrogen in PANI charges the adsorbent surface positively, whereas the SO_3^- group charges the adsorbate RB19 negatively. As a result, electrostatic interactions constitute the predominant propelling factor in most adsorption processes, especially those using surface-modified adsorbents as shown in Fig. 1. Modifications are made to increase surface characteristics or charge, facilitating adsorption. Here PANI is modified by loading CuBTC on its surface. The RB19 stock solution (1000 ppm) was dissolved in deionized water. The adsorption of RB19 dye on PANI/CuBTC nanoparticles was examined. The ideal experimental conditions for removal efficiency were investigated: a stirrer was used to agitate 10 mL of 60 ppm dye solution (RB19) and a known quantity of adsorbent (0.3–0.9 g L^{-1}) at a temperature ranging from 30 °C to 50 °C for a specific period (10 to 60 min) in the dark. Following this, the supernatant solutions were analyzed using a UV-visible spectrophotometer to calculate the residual concentrations of RB19 at 593 nm wavelength. The starting and final dye concentrations were used to compute the dye removal efficiency, according to eqn (1):

$$\text{Removal efficiency, } R(\%) = \frac{C_{\text{initial}} - C_{\text{final}}}{C_{\text{initial}}} \times 100 \quad (1)$$

where C_{initial} is the adsorbate's initial concentration and C_{final} is its final concentration. All the tests were performed thrice, and the average values were taken into account.

3. Results and discussion

3.1 Adsorbent characterization

The X-ray diffraction (XRD) patterns for both the individual materials and the nanocomposites are shown in Fig. 2(a). The peaks seen at 2θ ~6.72 (200), 9.46 (220), 11.6 (222), 13.44 (440), 14.64 (422), 17.46 (511), 19.02 (440), 20.22 (660), 25.92 (730), 29.34 (751), 36.4 (773), 39.14 (828), and 47.14 (751) confirm the formation of CuBTC. CuBTC likely possesses a crystalline structure due to the presence of distinct sharp peaks. The presence of a peak at 25.26 (003) indicates that PANI has a polymeric nature. However, the amorphous nature of PANI is confirmed by the peaks at 2θ ~14.84 (121), 20.63 (310), and 25.26 (003).[35] The nanocomposites also displayed both types of peaks. No more impurity peak was seen, indicating that the composites were effectively produced.

BET analysis was used to calculate the average pore size, total surface area, and total pore volume of nanocomposites as well as the individual materials, as shown in Fig. 2(b and c). CuBTC showed a type I isotherm whereas PANI displayed a type IV isotherm. Due to the higher content of PANI in the nanocomposites, they exhibited a type IV isotherm, indicating the presence of multiple layers of adsorbed molecules and the condensation of certain molecules within the small capillary pores of the adsorbent. Various surface parameters were calculated using the BJH plots and are summarized in Table 1. The 10CP nanocomposite has the greatest pore diameter in comparison to any of the other synthesized nanocomposites and bare materials which is a favorable characteristic for better adsorption.

FESEM analysis has been instrumental for comprehending the morphological characteristics of the synthesized nanocomposite. The FESEM images reveal key insights: CuBTC exhibits a crystalline octahedral structure (Fig. 3(a)), while PANI displays a fibrous morphology with a porous nature (Fig. 3(b)). In contrast, the nanocomposite features both these morphologies simultaneously, indicating successful heterojunction formation (Fig. 3(c)). This dual morphology offers numerous active sites, significantly increasing the catalyst's surface area for enhanced pollutant adsorption capability. Additionally, EDS examination revealed the presence of C, N, O, Cu, and Cl in our composite (Fig. 3(d)). The elemental color mapping in the picture emphasizes the uniform spread of these components, further boosting the composite's efficacy in adsorption (Fig. 3(e)).

X-ray photoelectron spectroscopy (XPS) was used to examine the materials' core electron binding energies, elemental composition, and oxidation states. The survey spectra of the

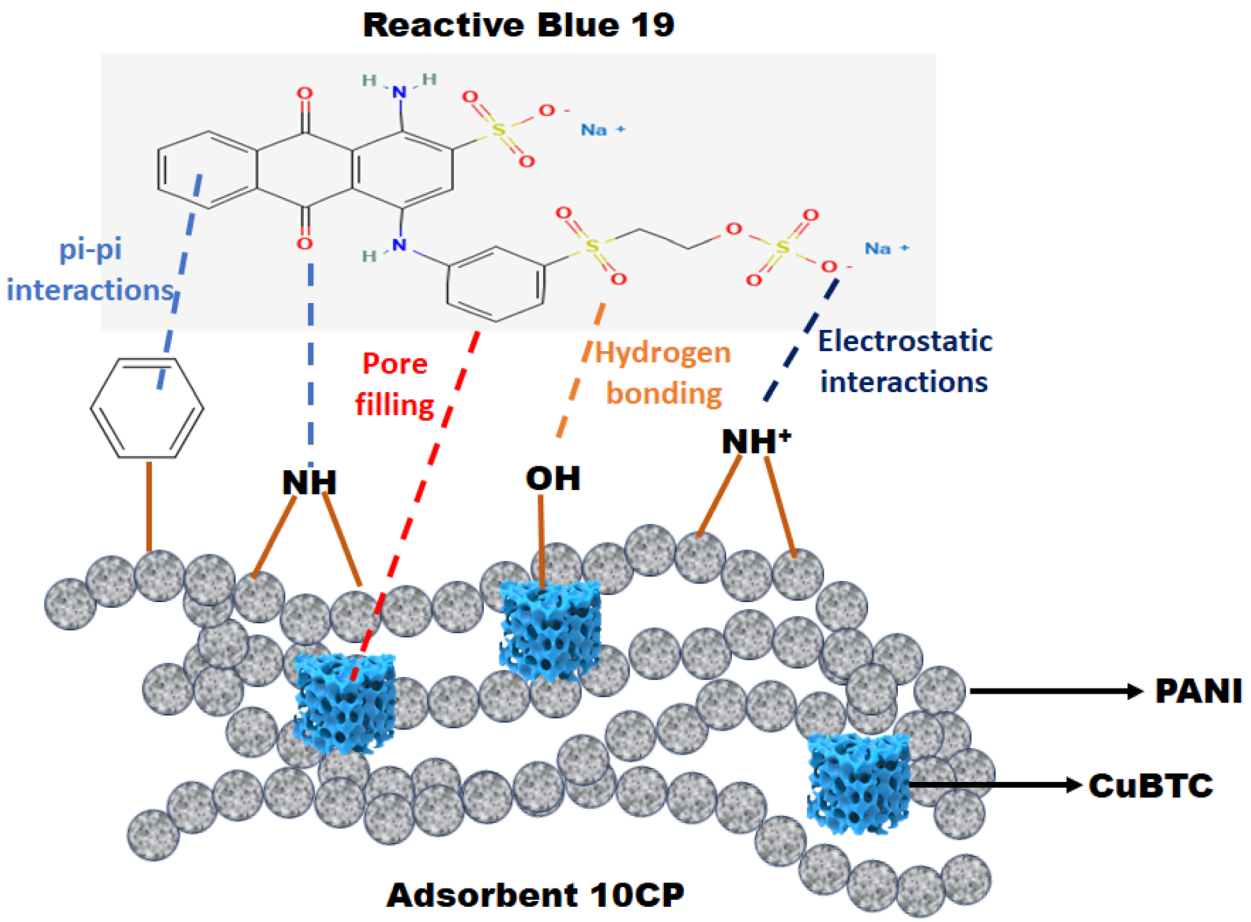

Fig. 1 Interactions between RB19 dye and the PANI/CuBTC nanocomposite.

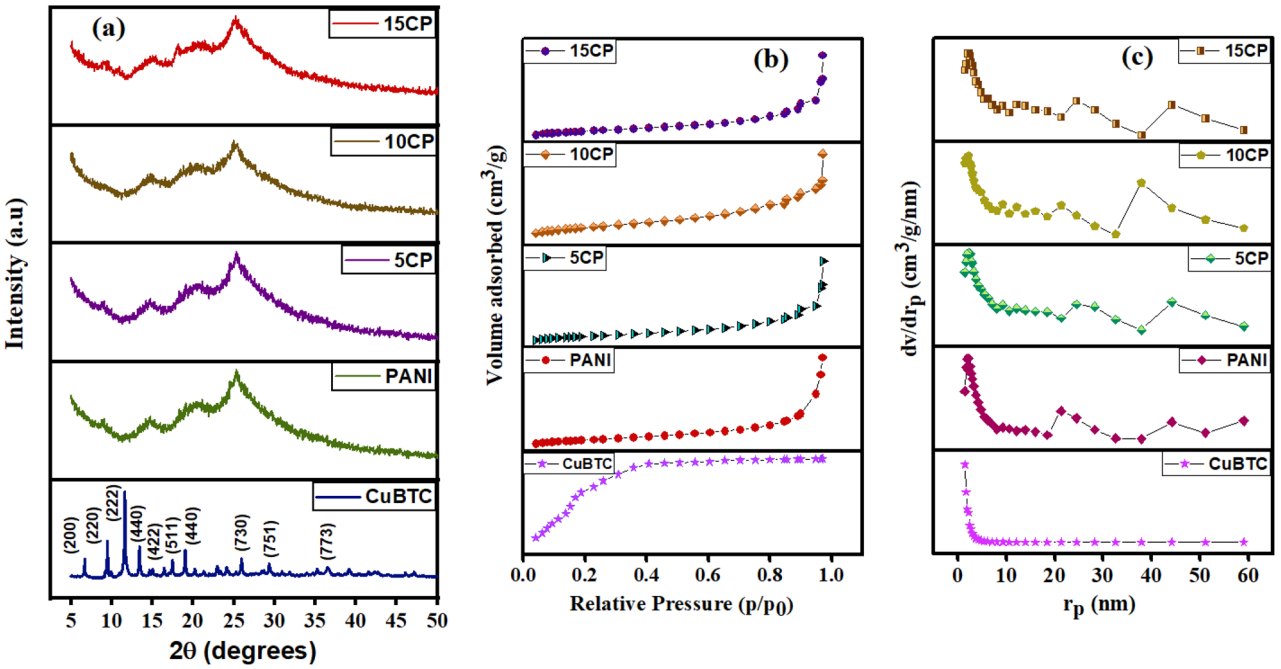

Fig. 2 (a) XRD spectra of CuBTC, PANI, and the nanocomposites, (b) BET surface area isotherms, and (c) BJH plots.

Table 1 BET table depicting the surface area, pore diameter and mean pore volume

Sample code	Pore diameter (nm)	Specific surface area ($m^2\ g^{-1}$)	Mean pore volume ($cm^3\ g^{-1}$)
CuBTC	1.754	1280	0.563
PANI	13.775	18	0.062
5CP	13.082	70.8	0.242
10CP	14.346	74	0.259
15CP	13.282	52.8	0.175

composite are presented (Fig. 4(a)). The peaks indicate that the main components of the 10CP composite are carbon, oxygen, and nitrogen. To analyze this, deconvolution was carried out using a least-squares Gaussian fitting model. In the C 1s spectra (Fig. 4(b)), two peaks at around 284 eV and 285 eV are attributed to C–C and C–H bonds, respectively. Another peak at 288 eV is likely linked to C=O, pointing to the presence of BTC. For the O 1s spectra (Fig. 4(c)), two peaks at 533 eV and 531.2 eV were identified, which are associated with oxygen in water and BTC.[36] The N 1s spectra (Fig. 4(d)) displayed three distinct peaks, each representing different nitrogen environments: one at 398.59 eV for quinoid amine, another at 398.95 eV for benzenoid amine, and a third at 400.58 eV corresponding to the nitrogen cationic radical (N^+).[37] In the Cu 2p spectrum, the peak at 934.3 eV corresponds to Cu(II) in the Cu $2p_{3/2}$ state, while the one at 954.9 eV is associated with Cu(II) in the Cu $2p_{1/2}$ state (Fig. 4(e)). Shake-up satellites were also detected in the 960–964 eV and 940–945 eV regions.[38]

FTIR spectra of individual materials and the nanocomposites are given in Fig. S(1).† CuBTC displays distinct signals at various wavenumbers, reflecting its structural characteristics. Starting from lower wavenumbers, the benzene ring's out-of-plane C–H bending vibrations are observed at 735 and 763 cm^{-1}, indicating the presence of dicarboxylate groups. At 1120 cm^{-1}, a C–O–Cu vibration associated with the MOF is noted. Moving to higher wavenumbers, the spectrum features a symmetric stretch of BTC carboxylate groups at 1373 cm^{-1} and an asymmetric stretch at 1451 cm^{-1}. Additionally, peaks at 1642 and 1588 cm^{-1} correspond to asymmetric vibrations in $-CO_2-$ groups. The C=O stretch appears at 1730 cm^{-1}, and finally, a broad signal at 3351 cm^{-1} indicates O–H stretching from adsorbed water molecules. This array of signals provides insight into the various functional groups and bonding interactions present in CuBTC.[39] In the FTIR spectrum of PANI, a broad peak at 3422 cm^{-1} is observed, which is attributed to the stretching of $-NH_2$ groups. A C–H stretching vibration is seen at 2924 cm^{-1}, while C–N stretching appears at 1307 cm^{-1}. Additionally, the peak at 1580 cm^{-1} is of a benzoid ring. Additionally, the peak at 1456 cm^{-1}, associated with C=C vibrations in the aromatic ring, indicates the formation of polymer chains. The 1297 cm^{-1} peak is attributed to C–N bond stretching in aromatic systems. Peaks seen between 1128 cm^{-1} and 1225 cm^{-1} are linked to the protonation of PANI.[40] The nanocomposite peaks associated with different groups may show small variations in wavenumber. This confirms the effective production of the composites.

3.2 Influence of CuBTC loading on PANI

Modification of PANI with CuBTC increases the number of active sites. As the quantity of CuBTC increases, so does the proportion of RB19 removed, increasing from 57% with 5CP to 62.3% with 10CP. However, increasing the CuBTC level in the

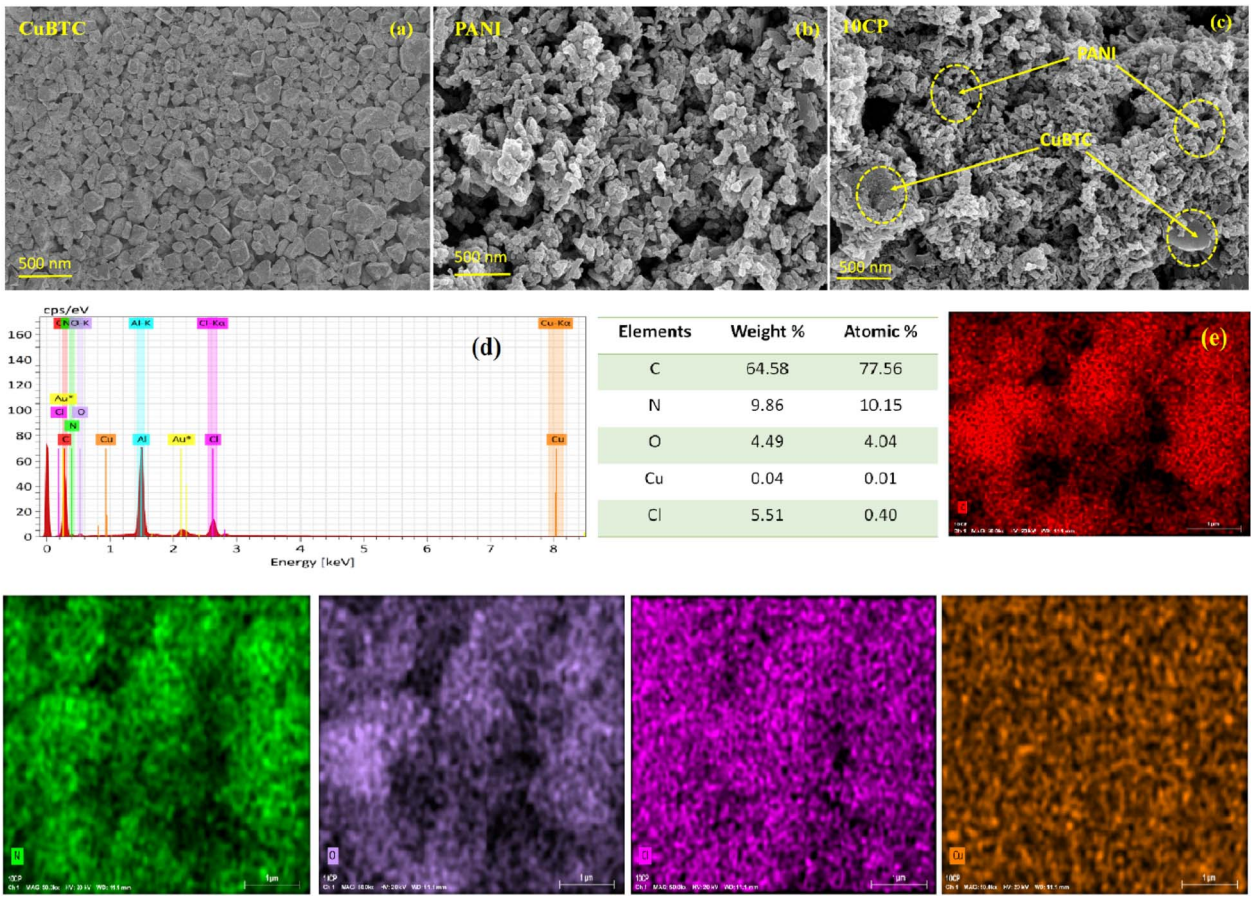

Fig. 3 The FE-SEM images show (a) CuBTC, (b) PANI, and (c) 10CP, (d) the EDS analysis of 10CP, and (e) the color mapping for 10CP.

adsorbent reduces the removal rate to 58%. This decrease might be attributable to the filling of the active pockets in the adsorbent. Hence, 10CP is considered the best weight ratio for the adsorption experiments. Fig. 5(a) illustrates the percentage of RB19 removal using various PANI/CuBTC adsorbents.

3.3 Influence of time

To examine the impact of contact time on RB19 adsorption, the concentration of RB19 was kept constant at 60 mg L^{-1}, while the adsorbent concentration was takens 4 g L^{-1} (Fig. 5(b)). As contact duration increased, RB19 elimination increased from 28.4% to 77.8%, improving adsorption capacity. The initial adsorption of RB19 was rapid, owing to the abundant active sites on the surface of 10CP, which play a key role in wastewater purification. Maximal adsorption occurs in 50 minutes, after which adsorption equilibrium is reached, resulting in the steady removal of RB19. As a result, 50 minutes of contact time was employed for further analysis.

3.4 Influence of pH

The adsorption of RB19 onto the surface of 10CP is significantly influenced by the pH of the solution. In order to investigate this, the adsorption process was examined throughout the pH range of 1 to 12, with 0.1 M HCl and 0.1 M NaOH solutions used to modify the pH. The elimination effectiveness of RB19 increased from 75.74% to 89.7% as the pH increased from 1 to 2. This improvement is attributed to the H^+ ions, which facilitate attraction by electrostatic forces between the cationic nitrogen on the adsorbent surface and the negatively charged RB19 molecules, enhancing adsorption. However, in the pH range of 3 to 12, the removal efficiency decreased to 56.5%. This drop is caused by the removal of a proton from the surface of PANI in the solution, which diminishes the interaction between the 10CP material and the RB19 dye. Therefore, pH changes have an important effect on the adsorption of RB19 onto 10CP primarily influencing the ionic attractive forces between the 10CP surface and the RB19 molecules dissolved in the solution. The solution's pH 2 yielded the highest percentage of adsorption (89.7%) (Fig. 5(c)). The 10CP surface's zero-charge state indicated as pH_{pzc}, was determined to be 3.44 which represents the pH at which the net surface charge of the material is zero (Fig. 5(d)).

3.5 Influence of temperature

While holding all other parameters constant, the adsorptive removal of RB19 dye employing the 10CP material was studied over the temperature range of 30 °C to 50 °C (Fig. 6(a)). It was found that as temperature increases, the adsorption of RB19 also increases, suggesting that higher temperatures enhance the

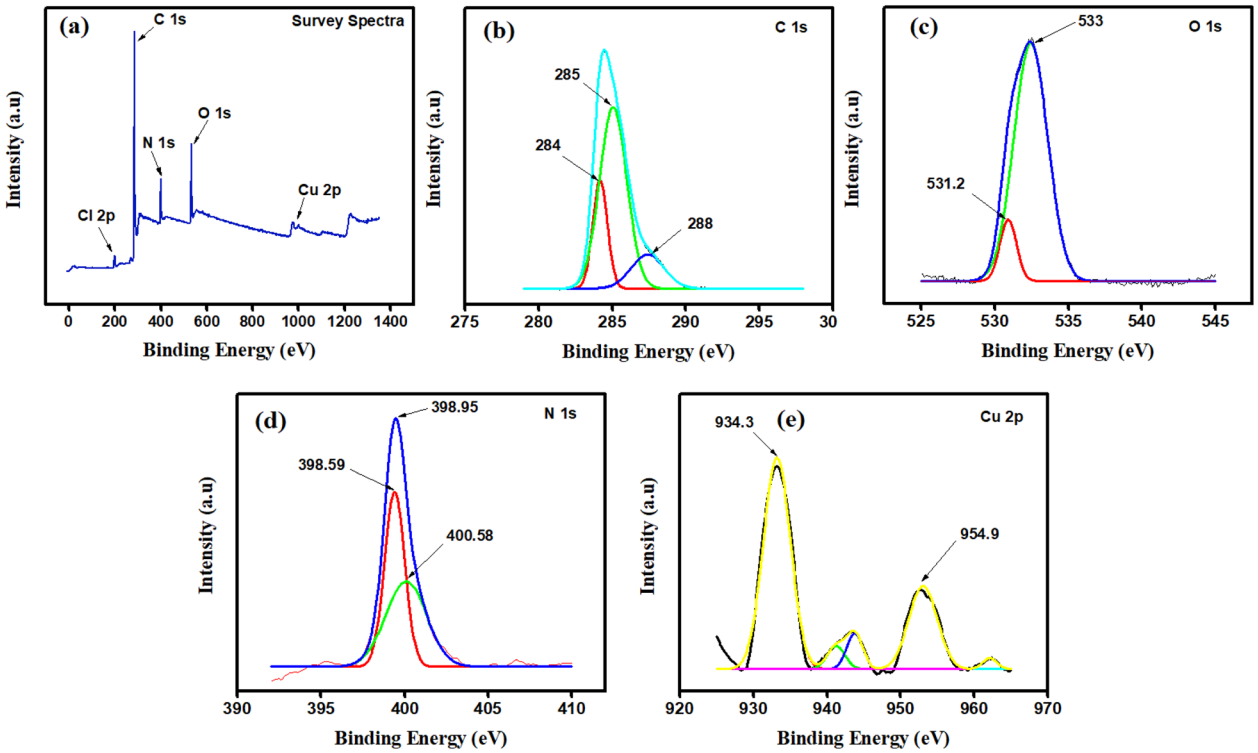

Fig. 4 (a) The survey spectrum, (b) XPS spectra of the C 1s core level, (c) XPS spectra of the O 1s core level, (d) XPS spectra of the N 1s core level, and (e) Cu 2p core level XPS spectra.

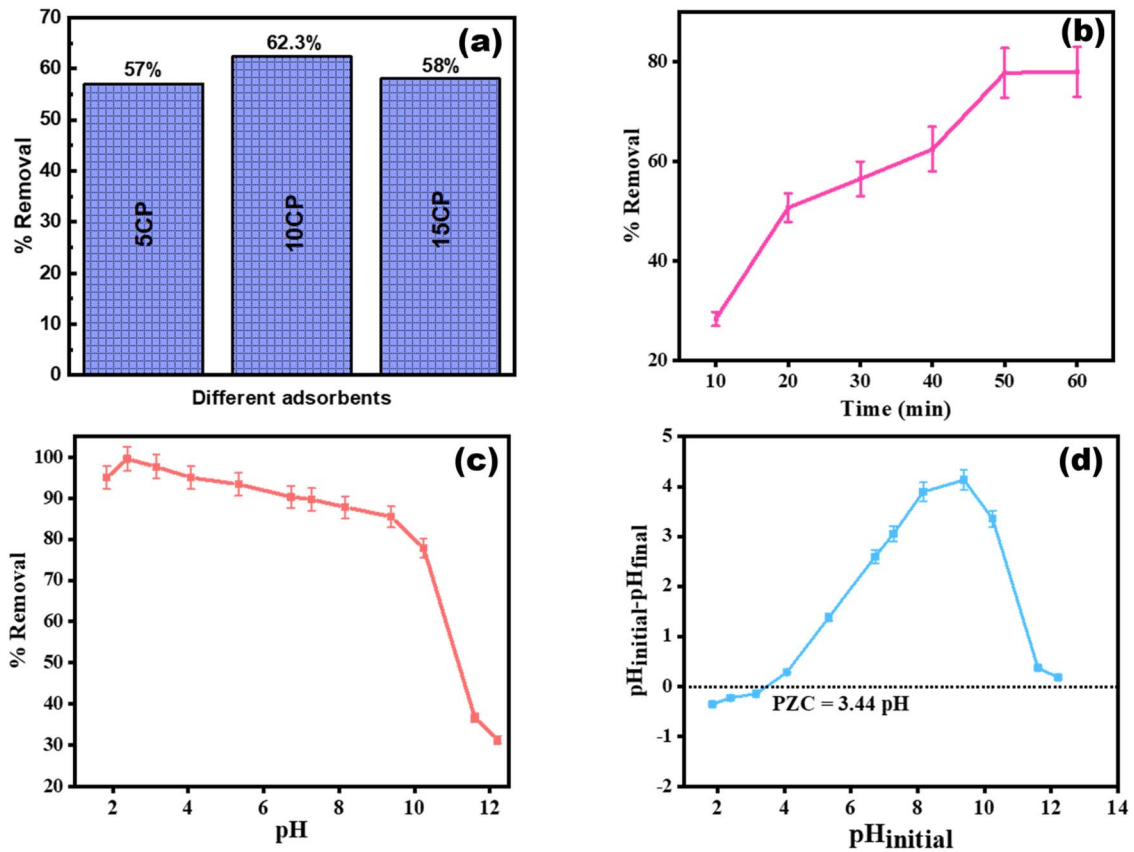

Fig. 5 (a) Comparison between different PANI/CuBTC adsorbents, (b) time optimization studies, (c) pH optimization studies, and (d) pzc studies.

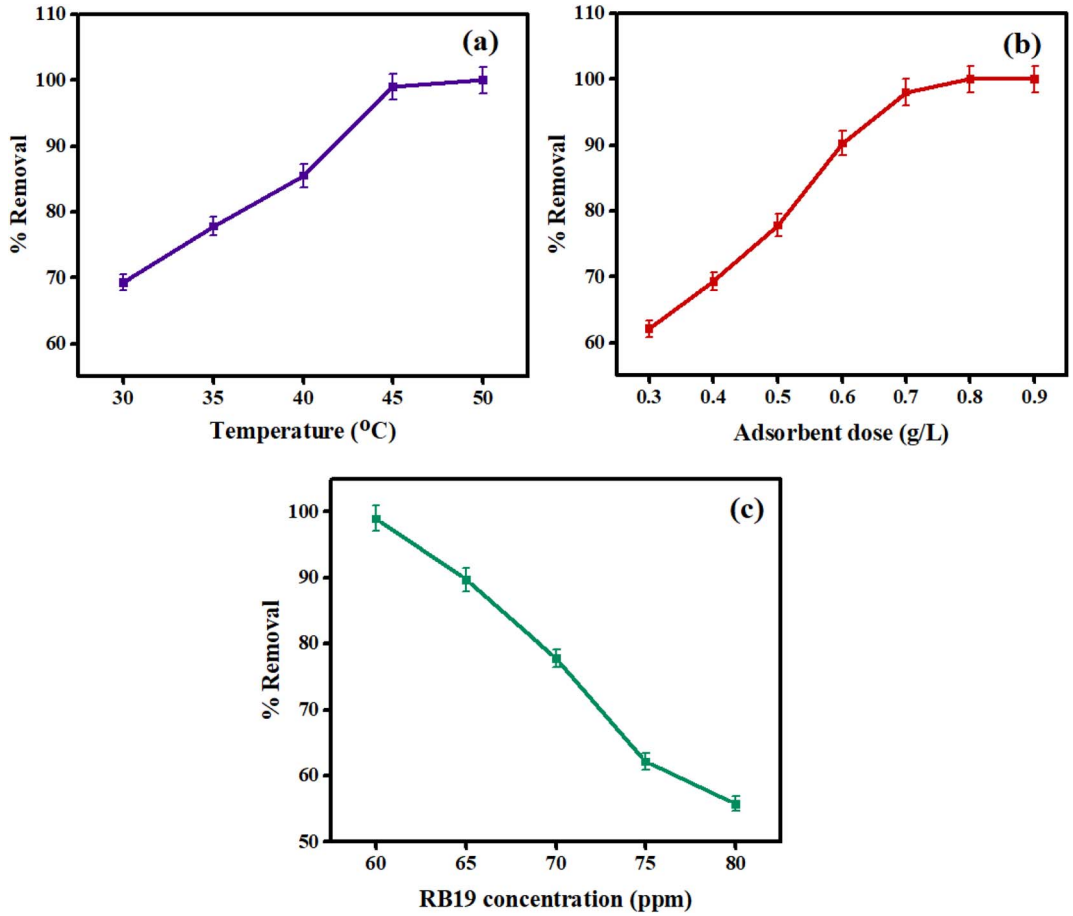

Fig. 6 (a) Temperature studies, (b) adsorbent dose studies, and (c) influence of concentration of RB19 dye.

adsorption process. The adsorption of RB19 onto 10CP is characterized as endothermic. The highest removal efficiency of RB19 (93.4%) was observed at 50 °C, where the molecules gained sufficient thermal energy to effectively interact with the adsorption sites on the surface of the adsorbent. In contrast, at lower temperatures, the molecules lacked enough energy to fully engage with these sites. Based on these results, a temperature of 50 °C was chosen for all further adsorption experiments, as it provided the most favorable conditions for RB19 removal using 10CP.

3.6 Influence of adsorbent dose

We performed experiments with an initial RB19 concentration of 60 mg L^{-1}, a pH of 2, and a contact time of 50 minutes to evaluate the effect of different dosages of 10CP on RB19 dye removal. According to Fig. 6(b), as the amount of adsorbent increased from 3 mg to 9 mg, there was a corresponding rise in the percentage removal of RB19, reaching a peak of 99% at 8 mg, after which it stabilized. This initial increase in removal percentage is likely attributed to the higher surface area of the adsorbent and the greater availability of active sites for adsorption.

3.7 Influence of the initial concentration of RB19 dye

Fig. 6(c) depicts the association between the initial RB19 concentration and the percentage of elimination. The percentage clearance decreased (from 99% to 55.7%) when the starting concentration of RB19 increased from 60 mg L^{-1} to 80 mg L^{-1}. This decline occurs because higher initial concentrations lead to quicker attainment of adsorption equilibrium, driven by increased interaction forces between RB19 and adsorption sites until saturation occurs. Therefore, for optimal experimental conditions, an initial RB19 concentration of 60 mg L^{-1} was chosen, as it yielded the highest percentage removal in the liquid phase under the studied conditions.

3.8 Adsorption isotherms

From our experimental data, we derived several isotherms, including Freundlich, Langmuir, Halsey, Harkins–Jura, and Dubinin–Radushkevich (D–R).[41] The accuracy of these isotherms was assessed using the Pearson correlation coefficient (R^2).

3.9 Freundlich adsorption isotherm

The Freundlich adsorption isotherm describes the adsorption of molecules onto an adsorbent with surfaces that vary in their properties, allowing for the formation of multiple layers.[42] It can be expressed as the following eqn (2):

$$\log Q_e = \log K_f + \frac{\log C_e}{n} \quad (2)$$

The Freundlich constant K_f (expressed in the units of $mg^{1-1/n}$ $L^{1/n}$ g^{-1}) signifies the adsorption capacity, while 'n' indicates the intensity of adsorption.[43] A value of 'n' greater than 1 indicates favorable conditions for the adsorption process. Fig. 7(a) shows the linear fit of the Freundlich adsorption isotherm, illustrating the adsorption of RB19 onto 10CP.

3.10 Langmuir adsorption isotherm

The Langmuir isotherm model proposes that adsorption occurs on a homogeneous surface of the adsorbent, where molecules form a monolayer without interacting with each other.[44] The Langmuir isotherm can be illustrated as follows:

$$\frac{C_e}{Q_e} = \frac{1}{Q_m K_L} + \frac{1}{Q_m} C_e \quad (3)$$

In the Langmuir adsorption isotherm model, K_L denotes the affinity and binding site energy of the adsorbent (L mg^{-1}), which affects the strength of adsorption. Q_m refers to the maximum adsorption capacity, which indicates how much RB19 is absorbed per gram of adsorbent (mg g^{-1}). Additionally, the equilibrium adsorption capacity, Q_e (mg g^{-1}), is also calculated. To validate the Langmuir isotherm, a linear plot of C_e/Q_e *versus* C_e was created, allowing for the determination of Q_m and K_L from the graph's slope and intercept.[44] Fig. 7(b) shows the Langmuir isotherm plot for RB19 dye adsorption onto 10CP, highlighting how well this model captures the adsorption behavior.

The Langmuir adsorption isotherm's properties and feasibility were described using the separation factor or equilibrium parameter R_L (a dimensionless constant), as shown in the following eqn (4).

$$R_L = \frac{1}{K_L + C_o} \quad (4)$$

The R_L value is used to analyze the linearity of the adsorption process ($R_L = 1$), irreversibly unfavorable ($R_L > 1$), or favorable ($0 < R_L < 1$).[42] According to Fig. 7(c), R_L values were found to be less than 1 ($0 < R_L < 1$), indicating favorable conditions for the adsorption process.[45]

3.11 Harkins–Jura adsorption isotherm

The presence of heterogeneous pore distributions is addressed by the Harkins–Jura model and it also presents an outline for describing multilayer adsorption. Its linear form is expressed as follows:[46]

$$\frac{1}{Q_e^2} = \frac{B}{A} - \frac{1}{A} \log C_e \quad (5)$$

In Fig. 7(d), the values of constants A and B are obtained from the slope and intercept of this equation.

3.12 Halsey adsorption isotherm

This isotherm is particularly suited to model the multilayer adsorption process that takes place on heterogeneous, porous solids.[46] As shown in Fig. 7(e), these processes are defined by plotting $\ln Q_e$ *versus* $\ln C_e$.

$$\ln Q_e = \frac{1}{K} \ln K - \frac{1}{n} \ln C_e \quad (6)$$

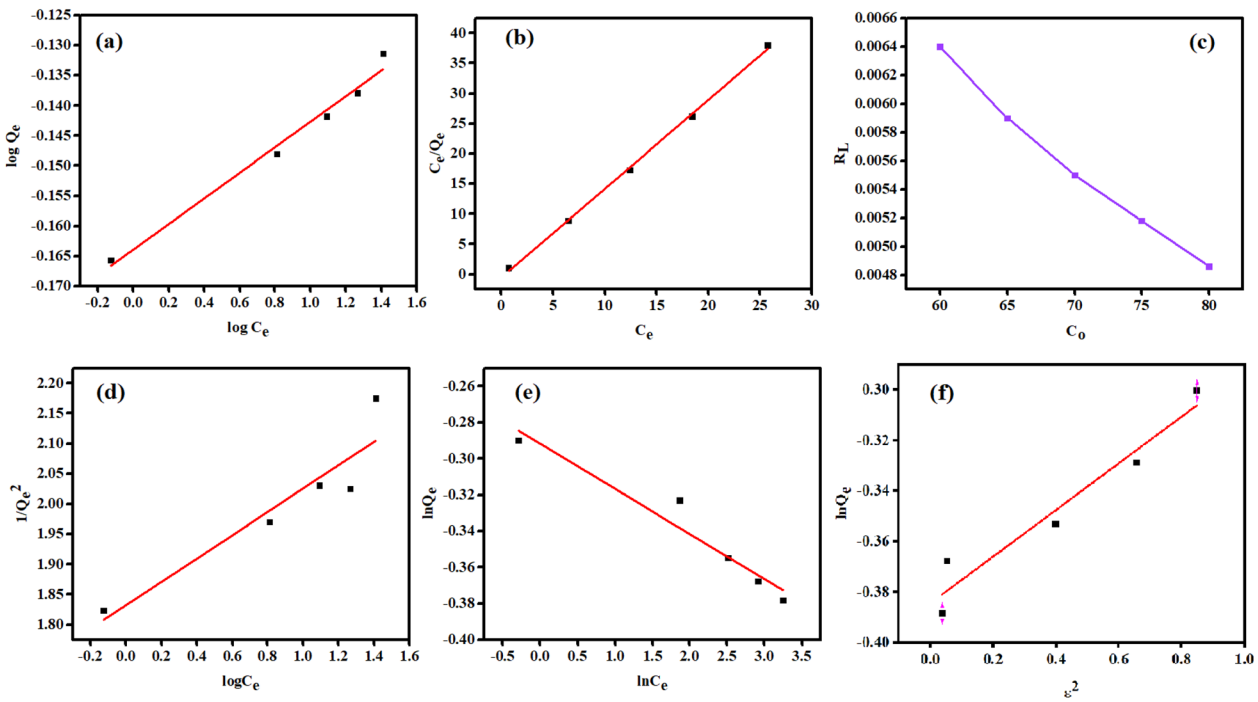

Fig. 7 (a) Freundlich model, (b) Langmuir isotherm, (c) equilibrium parameter R_L, (d) Halsey isotherm, (e) Harkins–Jura isotherm, and (f) D–R isotherm.

Table 2 Table for parameters of various isotherms

S. no.	Models	Parameters	Values for RB19
1	Langmuir isotherm	K_L (L mg^{-1})	2.557
		Q_m (mg g^{-1})	0.678
		R^2	0.998
2	Freundlich isotherm	K_F (mg$^{1-1/n}$ L$^{1/n}$ g^{-1})	1.458
		$1/n$	0.021
		R^2	0.983
3	Harkins–Jura	A	5.170
		B	9.473
		R^2	0.869
4	Halsey	$1/n$	0.024
		K (mg L^{-1})	1.223×10^{-5}
		R^2	0.940
5	Dubbin–Radushkevich	B [(mol J^{-1})^2]	9.23×10^{-2}
		Q_s (mg g^{-1})	1.468
		R^2	0.939

3.13 Dubinin–Radushkevich (D–R) model

This model operates by assuming that adsorption occurs without a uniform surface, aligning with Polanyi's potential theory.[47] Eqn (7) below represents the linear form of the D–R isotherm equation.[47]

$$\ln Q_e = \ln Q_s - B\varepsilon^2 \quad (7)$$

In eqn (8) below, ε represents the Polanyi potential, B is the constant that indicates the mean adsorption energy, and Q_s denotes the theoretical adsorption capacity.[46]

$$\varepsilon = RT \ln\left(1 + \frac{1}{C_e}\right) \quad (8)$$

The parameters B and Q_s were determined from the plot of ln Q_e *versus* ε^2, where R represents the ideal gas constant and T (K) denotes the absolute temperature (Fig. 7(f)). Table 2 lists the parameters of these various isotherm models.

3.14 Adsorption kinetics

To explore the adsorption kinetics of RB19 on 10CP, several models were examined. The pseudo-first-order model, in particular, assumes that the adsorption rate is directly related to the number of available vacant sites. The linearized form of this model is presented below:[48]

$$\log(Q_e - Q_t) = \log(Q_e) - \frac{K_1}{2.303} \times t \quad (9)$$

The linear equation of the pseudo-second order kinetic model is formulated as follows:

$$\frac{t}{Q_t} = \frac{1}{K_2 + {Q_e}^2} + \frac{t}{Q_e} \quad (10)$$

Q_e is the equilibrium quantity of RB19 adsorbed (mg g^{-1}), whereas Q_t is the total amount of RB19 adsorbed at time t (minute). The adsorption rate constant, K_1 (L min^{-1}), may be calculated from the slope of a graph plotting $\log(Q_e - Q_t)$ *versus* t,[48] as illustrated in Fig. 8(a). The rate constant K_2 (g mg^{-1} min^{-1}), specific to the pseudo-second-order model, is obtained from the slope and intercept of the plot of t/Q_t *versus* time t,[49] as given in Fig. 8(b).

The Elovich isotherm model effectively describes adsorption processes occurring on adsorbents with energetically diverse surfaces. The equation for the Elovich model is expressed as follows:

$$Q_t = \frac{1}{B}\ln(ab) + \frac{1}{B}\ln(t) \quad (11)$$

The equilibrium rate parameter 'a' (mg g^{-1} min^{-1}) indicates the initial adsorption rate, whereas 'b' (g mg^{-1}) is related to desorption,[46] as determined from the plot of Q_t against ln t, as illustrated in Fig. 8(c). Weber and Morris developed the intra-particle diffusion kinetic model,[46] which describes how adsorption occurs within porous adsorbents.

$$Q_t = K_i t^{1/2} + C_i \quad (12)$$

k_i (mg g^{-1} min$^{-1/2}$) is the rate constant and the parameter 'C_i' is determined from the plot of Q_t against t, as depicted in Fig. 8(d). Table 3 contains all the parameters from these various kinetic models. The analysis revealed that the pseudo-second-order model had the highest regression coefficient compared to other kinetic models, suggesting that chemisorption predominantly controls the adsorption process.[49]

3.15 Thermodynamic investigation

Thermodynamic parameters were calculated using eqn (13), while the van't Hoff eqn (14) was employed to estimate $\ln(Q_e/C_e)$:[48]

$$\ln\frac{Q_e}{C_e} = -\frac{\Delta H}{RT} + \frac{\Delta S}{R} \quad (13)$$

$$\Delta G^\circ = \Delta H^\circ - T\Delta S^\circ \quad (14)$$

The amount of RB19 adsorbed per gram of adsorbent, denoted as Q_e (mg g^{-1}), depends on the equilibrium concentration C_e.

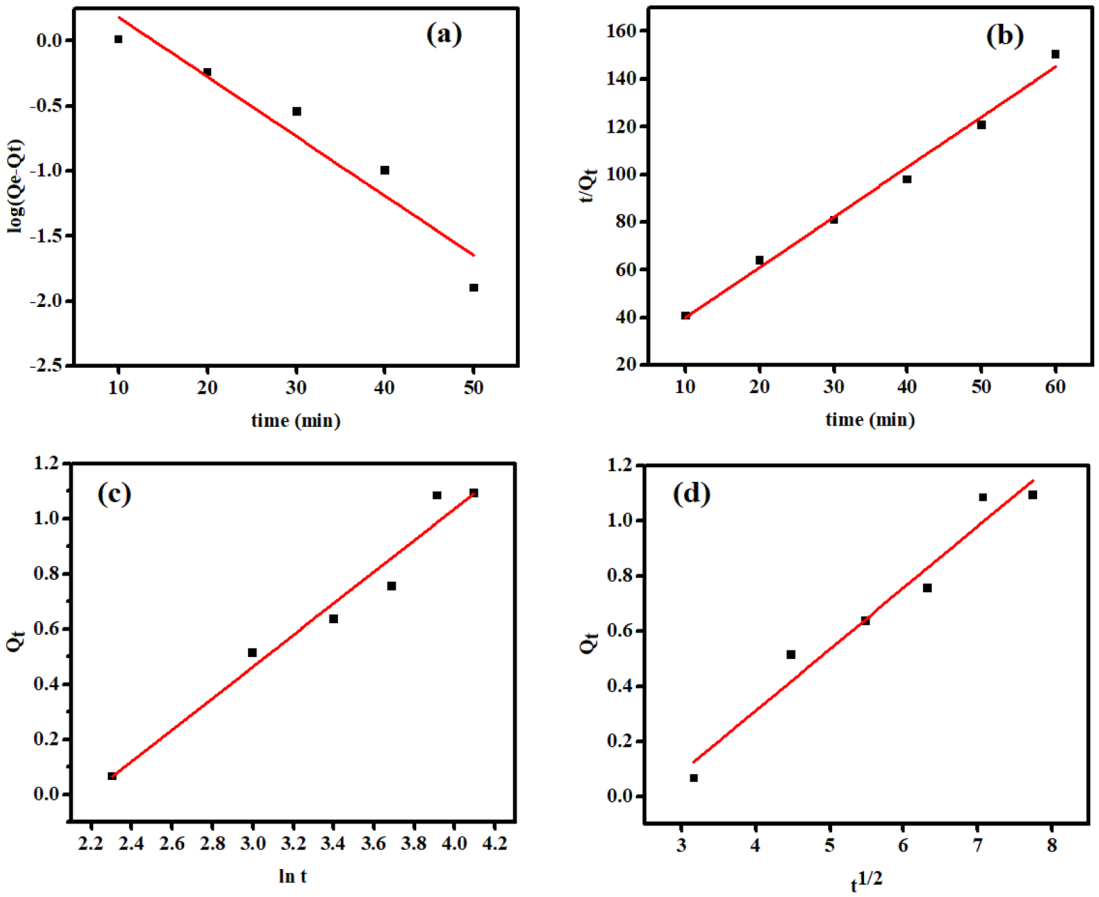

Fig. 8 Plots for various kinetic models: (a) pseudo first-order, (b) pseudo-second order, (c) Elovich and (d) intra-particle diffusion.

Table 3 Kinetic model parameters for adsorption of dye- RB19

S. no.	Kinetic model	Parameters	Values for RB19
1	Pseudo first order	k_1 (min^{-1})	0.105
		Q_e ($mg\ g^{-1}$)	4.37
		R^2	0.925
2	Pseudo second order	K_2 ($mg\ g^{-1}\ min^{-1}$)	0.172
		Q_e ($g\ mg^{-1}$)	0.475
		R^2	0.990
3	Elovich	a ($mg\ g^{-1}\ min^{-1}$)	47.7
		b ($g\ mg^{-1}$)	0.009
		R^2	0.964
4	Intra particle diffusion	C_i ($mg\ g^{-1}$)	−0.579
		K_i ($mg\ g^{-1}\ min^{-0.5}$)	0.222
		R^2	0.960

The gas constant, R, is 8.314 J mol^{-1} K^{-1}, and T represents the temperature in Kelvin. To determine $\Delta H°$ and $\Delta S°$, we plotted $\ln(Q_e/C_e)$ against $1/T$,[48] as depicted in Fig. S(2).† $\Delta G°$ values were calculated at temperatures of 298, 303, 308, and 313 K using eqn (14), corresponding to the experimental conditions. The negative $\Delta G°$ values listed in Table 4 indicate the spontaneity and thermo-dynamical favourability of the adsorption process.[42] A positive $\Delta S°$ suggests increased affinity of the adsorbent towards RB19 and greater disorderness.[46] The positive $\Delta H°$ value indicates that the adsorption process absorbs heat, making it endothermic.[48] Comparative percentages of pollutant removal by different materials are summarized in Table 5, indicating that polyaniline and MOF-based adsorbents show promise for effectively removing toxic pollutants.

3.16 Reusability studies

Besides assessing how well a nanocomposite adsorbs, it's crucial to determine its durability for practical use. To evaluate this, the 10CP nanocomposite underwent repeated recycling tests to study its stability and consistency. The objective was to analyze how it adsorbs RB19 under the same experimental conditions over multiple reaction cycles. After each cycle, the catalyst was subjected to centrifugation, washing, and drying before being reused. According to the findings in Fig. S(3),† regardless of the ten consecutive cycles of adsorption, effectiveness remained at 80%. This suggests that 10CP can be reused effectively as a catalyst. Removal effectiveness decreased from 100% to 80% which can be attributed to the inevitable loss of some catalysts during retrieval. Furthermore, untreated intermediates may stick to the catalyst surface, potentially blocking active sites and decreasing efficiency. To investigate this, FTIR spectra of 10CP were recorded both before and after

Table 4 Values of various thermodynamic parameters

Temperature (K)	Gibbs free energy ΔG (kJ mol^{-1})	Enthalpy change ΔH (J mol^{-1})	Entropy change ΔS (J mol^{-1} K^{-1})	R^2
303	−1.728	795.15	3.082	0.994
308	−1.744			
313	−1.759			
318	−1.775			
323	−1.790			

Table 5 List of various nanocomposites for the adsorption of RB19 dye reported in the literature

Pollutant	Adsorbent	Initial concentration of the pollutant (mg L^{-1})	% Adsorption	Reference
RB19	PANI/nickel ferrite	30	95.2	50
RB19	CS-MHAP	50	93	51
RB19	AC-ZnO	25	99	52
RB19	Fe_3O_4@L-arginine	50	96.34	53
RB19	MgO	50	99	54
RB19	CuBTC/PANI	60	99	Present work

the dye adsorption process (Fig. S(4)†). After comparing we observed that the peak corresponding to the OH stretching frequency disappeared after the adsorption of RB19 dye, which further indicates the presence of hydrogen bonding interactions between the dye and the adsorbent surface. After ten cycles, the nanocomposite was characterized by XRD analysis, where it was seen that there is a slight decrease in the intensity of the peak due to the absorption of the dye molecule on the catalyst surface but there is no change in the XRD pattern of the catalyst (Fig. S(5)†).

4. Conclusion

The CuBTC/PANI adsorbent was created using both hydrothermal and polymerization methods to effectively remove RB19 dye from water. Among various concentrations tested, the 10CP adsorbent demonstrated the best removal efficiency. To optimize the adsorption process, factors like contact time, dosage, dye concentration, pH and temperature were carefully analyzed through experiments. The adsorption data adhered to the Langmuir isotherm model, suggesting that the dye molecules form a monolayer on the surface of the adsorbent. Kinetic studies revealed a fast dye removal rate, most accurately described by the pseudo-second-order model, which implies that chemisorption is influenced by both the dye and adsorbent concentrations. Thermodynamic analysis showed that the process is spontaneous and becomes more efficient at higher temperatures. In conclusion, while the CuBTC/PANI composite exhibits promising dye removal capabilities, certain limitations should be acknowledged to provide a balanced perspective on its applicability. One aspect to consider in the application of CuBTC/PANI for dye removal is its performance under real industrial wastewater conditions. While the composite has demonstrated excellent adsorption efficiency in controlled laboratory settings, the presence of other contaminants, such as salts, organic matter, and suspended solids in industrial effluents, may lead to pore blocking, potentially affecting its adsorption capacity over time. Additionally, optimizing the synthesis process for large-scale production could further enhance its commercial viability. These considerations open avenues for future research, ensuring the material's adaptability and efficiency in diverse and complex wastewater treatment applications.

Data availability

The data supporting the findings of this study, including characterization results, adsorption and degradation kinetics, and isotherm studies, are presented within the article and the ESI† file accompanying it.

Author contributions

Bhavika Garg: visualization, writing – original draft, Palkaran Sethi: visualization, writing – original draft, and Soumen Basu: supervision.

Conflicts of interest

The authors declare no conflict of interest in the conduct of this study and the publication of its results.

Acknowledgements

We are grateful to DCBC and DPMS TIET for providing us with characterization facilities, and we are also thankful to Dr Akansha Mehta for XPS characterization.

References

1 M. Lakhane, M. Mahabole, K. Bogle, R. Khairnar and V. Kokol, *Fibers Polym.*, 2019, **20**, 2127–2139.
2 S. Chowdhury, R. Mishra, P. Saha and P. Kushwaha, *Desalination*, 2011, **265**, 159–168.
3 L. Dutta, G. K. Sethi and S. Dey, *Korean J. Chem. Eng.*, 2024, **41**, 589–607.
4 M. Ghaedi, S. Hajati, F. Karimi, B. Barazesh and G. Ghezelbash, *J. Ind. Eng. Chem.*, 2013, **19**, 987–992.
5 M. Visa, C. Bogatu and A. Duta, *Appl. Surf. Sci.*, 2010, **256**, 5486–5491.
6 F. A. Pavan, E. C. Lima, S. L. P. Dias and A. C. Mazzocato, *J. Hazard. Mater.*, 2008, **150**, 703–712.
7 Y. Hao, Z. Wang, J. Gou and S. Dong, *Arabian J. Chem.*, 2019, **12**, 3064–3074.
8 S. Agrawal, D. Tipre, B. Patel and S. Dave, *Process Biochem.*, 2014, **49**, 110–119.
9 A. Tadjarodi, M. Imani and M. Salehi, *RSC Adv.*, 2015, **5**, 56145–56156.
10 M. Malakootian, H. Hossaini, A. Asadipour and M. Daneshkhah, *Appl. Water Sci.*, 2018, **8**, 174.
11 S. F. Azha, A. L. Ahmad and S. Ismail, *Desalin. Water Treat.*, 2015, **55**, 956–969.
12 B. Garg, P. Hait and S. Basu, *J. Environ. Manage.*, 2024, **370**, 122403.
13 V. M. Vasconcelos, C. Ponce-de-León, S. M. Rosiwal and M. R. V. Lanza, *ChemElectroChem*, 2019, **6**, 3516–3524.
14 T. P. K. Murthy, B. S. Gowrishankar, R. H. Krishna, M. N. Chandraprabha and R. S. Rao, *Mater. Res. Express*, 2019, **6**, 055512.
15 F. Abdullah, A. R. Mohd Yusoff, W. A. Wan Abu Bakar, R. Ismail and A. Syafiuddin, *J. Chin. Chem. Soc.*, 2018, **65**, 1199–1209.
16 M. Tuzen, K. O. Saygi, C. Usta and M. Soylak, *Bioresour. Technol.*, 2008, **99**, 1563–1570.
17 T. C. Maponya, M. J. Hato, T. R. Somo, K. E. Ramohlola, M. D. Makhafola, G. R. Monama, A. Maity, K. D. Modibane and L. M. Katata-Seru, in *Trace Metals in the Environment - New Approaches and Recent Advances*, IntechOpen, 2021.
18 J. R. Baseri, P. N. Palanisamy and P. Sivakumar, *J. Chem.*, 2012, **9**, 1266–1275.
19 M. Rabbani, H. Kerdari and R. Rahimi, in *Proceedings of the 14th International Electronic Conference on Synthetic Organic Chemistry*, MDPI, Basel, Switzerland, 2010, p. 371.
20 D. Sompornpailin, C. Ratanatawanate, C. Sattayanon, S. Namuangruk and P. Punyapalakul, *Sci. Total Environ.*, 2020, **720**, 137449.
21 P. D'Ans, E. Courbon, A. Permyakova, F. Nouar, C. Simonnet-Jégat, F. Bourdreux, L. Malet, C. Serre, M. Frère and N. Steunou, *J. Energy Storage*, 2019, **25**, 100881.
22 S. Dhaka, R. Kumar, A. Deep, M. B. Kurade, S.-W. Ji and B.-H. Jeon, *Coord. Chem. Rev.*, 2019, **380**, 330–352.
23 Q. Yang, D. Chen, L. Chu and J. Wang, *J. Hazard. Mater.*, 2020, **389**, 122148.
24 M. S. Khan, Y. Li, D.-S. Li, J. Qiu, X. Xu and H. Y. Yang, *Nanoscale Adv.*, 2023, **5**, 6318–6348.
25 M. Shahnawaz Khan, M. Khalid and M. Shahid, *Mater. Adv.*, 2020, **1**, 1575–1601.
26 M. S. Khan, S. Zhu and S. B. Chen, *Chem. Eng. J.*, 2024, **500**, 157396.
27 E. Haque, J. E. Lee, I. T. Jang, Y. K. Hwang, J.-S. Chang, J. Jegal and S. H. Jhung, *J. Hazard. Mater.*, 2010, **181**, 535–542.
28 E. Haque, J. W. Jun and S. H. Jhung, *J. Hazard. Mater.*, 2011, **185**, 507–511.
29 C.-F. Zhang, L.-G. Qiu, F. Ke, Y.-J. Zhu, Y.-P. Yuan, G.-S. Xu and X. Jiang, *J. Mater. Chem. A*, 2013, **1**, 14329.
30 X. Liu, X. Li, W. Li, L. Liu, H. Ren, H. Jing, L. Zhang, J. Yin and L. Fan, *Microchem. J.*, 2024, **207**, 112127.
31 W. Li, L. Liu, X. Li, H. Ren, L. Zhang, M. K. Parvez, M. S. Al-Dosari, L. Fan and J. Liu, *J. Mater. Chem. B*, 2024, **12**, 11800–11809.
32 X.-Z. Guo, B. Lin, G.-Z. Xiong, R. Krishna, Z.-R. Zhang, Q.-Z. Liu, Z.-X. Zhang, L. Fan, J. Zhang and B. Li, *Chem. Eng. J.*, 2024, **498**, 154734.
33 S. Bordiga, L. Regli, F. Bonino, E. Groppo, C. Lamberti, B. Xiao, P. S. Wheatley, R. E. Morris and A. Zecchina, *Phys. Chem. Chem. Phys.*, 2007, **9**, 2676.
34 A. Kumar, R. Kumar and G. Pandey, *Macromol. Symp.*, 2018, **379**, 1600192.
35 P. Ahuja, S. K. Ujjain, I. Arora and M. Samim, *ACS Omega*, 2018, **3**, 7846–7855.
36 D. Xu, Y. Pan, M. Chen, Q. Pan, L. Zhu, M. Xue, D. Zhang, Q. Fang and S. Qiu, *RSC Adv.*, 2017, **7**, 26377–26383.
37 K. Zhang, L. L. Zhang, X. S. Zhao and J. Wu, *Chem. Mater.*, 2010, **22**, 1392–1401.
38 H. Li, J. Qin, Y. Zhang, S. Xu, J. Du and J. Tang, *RSC Adv.*, 2018, **8**, 39352–39361.
39 V. Jabbari, J. M. Veleta, M. Zarei-Chaleshtori, J. Gardea-Torresdey and D. Villagrán, *Chem. Eng. J.*, 2016, **304**, 774–783.
40 U. M. Chougale, J. V. Thombare, V. J. Fulari and A. B. Kadam, in *2013 International Conference on Energy Efficient Technologies for Sustainability*, IEEE, 2013, pp. 1078–1083.
41 M. Xu, Y. Zhang, Z. Zhang, Y. Shen, M. Zhao and G. Pan, *Chem. Eng. J.*, 2011, **168**, 737–745.
42 S. Agarwal, I. Tyagi, V. K. Gupta, N. Ghasemi, M. Shahivand and M. Ghasemi, *J. Mol. Liq.*, 2016, **218**, 208–218.
43 X. Tan, X. Wang, M. Fang and C. Chen, *Colloids Surf., A*, 2007, **296**, 109–116.
44 A.-H. Chen, C.-Y. Yang, C.-Y. Chen, C.-Y. Chen and C.-W. Chen, *J. Hazard. Mater.*, 2009, **163**, 1068–1075.
45 J. Niu, X. Jia, Y. Zhao, Y. Liu, W. Zhong, Z. Zhai and Z. Li, *Water Sci. Technol.*, 2018, **77**, 2327–2340.
46 N. Goyal, V. K. Bulasara and S. Barman, *J. Hazard. Mater.*, 2018, **344**, 417–430.
47 X. Tan, X. Wang, M. Fang and C. Chen, *Colloids Surf., A*, 2007, **296**, 109–116.
48 M. Sharma, D. Choudhury, S. Hazra and S. Basu, *J. Alloys Compd.*, 2017, **720**, 221–229.

49 M. Sharma, S. Hazra and S. Basu, *J. Colloid Interface Sci.*, 2017, **504**, 669–679.
50 M. R. Patil and V. S. Shrivastava, *Appl. Nanosci.*, 2015, **5**, 809–816.
51 V. C. Nguyen and Q. H. Pho, *Sci. World J.*, 2014, **2014**, 273082.
52 Y. Rashtbari, S. Afshin, A. Hamzezadeh, M. Abazari, Y. Poureshgh and M. Fazlzadehdavilb, *Desalin. Water Treat.*, 2020, **179**, 354–367.
53 A. Dalvand, R. Nabizadeh, M. Reza Ganjali, M. Khoobi, S. Nazmara and A. Hossein Mahvi, *J. Magn. Magn. Mater.*, 2016, **404**, 179–189.
54 J. Sharma, M. Sharma and S. Basu, *J. Environ. Chem. Eng.*, 2017, **5**, 3429–3438.